Publication Year	2018
Acceptance in OA@INAF	2020-10-13T10:48:32Z
Title	Simulating the optical performances of the LCLS bendable mirrors using a 2D physical optics approach
Authors	SPIGA, Daniele; Cocco, D.; Hardin, C. L.; Morton, D. S.; Ng, M. L.
DOI	10.1117/12.2323253
Handle	http://hdl.handle.net/20.500.12386/27760
Series	PROCEEDINGS OF SPIE
Number	10761

PROCEEDINGS OF SPIE

SPIEDigitalLibrary.org/conference-proceedings-of-spie

Simulating the optical performances of the LCLS bendable mirrors using a 2D physical optics approach

D. Spiga, D. Cocco, C. L. Hardin, D. S. Morton, M. L. Ng

D. Spiga, D. Cocco, C. L. Hardin, D. S. Morton, M. L. Ng, "Simulating the optical performances of the LCLS bendable mirrors using a 2D physical optics approach," Proc. SPIE 10761, Adaptive X-Ray Optics V, 1076107 (18 September 2018); doi: 10.1117/12.2323253

SPIE.

Event: SPIE Optical Engineering + Applications, 2018, San Diego, California, United States

Downloaded From: https://www.spiedigitallibrary.org/conference-proceedings-of-spie on 9/18/2018 Terms of Use: https://www.spiedigitallibrary.org/terms-of-use

Simulating the optical performances of the LCLS bendable mirrors using a 2D physical optics approach

D. Spiga[1,2], D. Cocco[1], C. L. Hardin[1], D. S. Morton[1], M. L. Ng[1]

[1]SLAC National Accelerator Laboratory, 2575 Sand Hill Road, 94025 Menlo Park (USA)
[2]INAF – Brera Astronomical Observatory, Via Bianchi 46, 23807, Merate (Italy)

ABSTRACT

The Linac Coherent Light Source (LCLS), a US Department of Energy Office of Science X-ray facility operated by the Stanford University, is being upgraded with a second source to provide eight beamlines (five existing and three under construction) with either high-repetition or high-intensity pulses and highly coherent X-ray beams. The photon transportation and distribution to each beamline relies on, among other elements, elliptically-bendable mirrors, often in Kirkpatrick-Baez (K-B) configuration. One of the crucial tasks in beamline design and performance prediction is the self-consistent simulation of the final point spread function of the complete optical system, simultaneously accounting for diffractive effects, mirror deformations, and surface finishing defects. Rather than using ray-tracing routines, which cannot manage diffractive effects, and rather than employing the first-order scattering theory, which cannot be applied when the optical path differences exceed the radiation wavelength, a wavefront propagation formalism can be used to treat all the aspects at the same time. For example, the WISE code, initially developed for astronomical X-ray mirrors at INAF-OAB, and subsequently used to simulate X-ray reflective systems at the Fermi light source, is now a part of the well-known OASYS simulation package. In this paper, we extend the model to a two-dimensional imaging and show performance simulations of two elliptical mirrors to form a complete Kirkpatrick-Baez system.

Keywords: Free-Electron Laser, LCLS, bendable mirrors, physical optics, diffraction

1. INTRODUCTION

The Linac Coherent Light Source (LCLS)[1] at SLAC national accelerator laboratory is being upgraded to improve its optical performances. A major reconstruction of the entire facility is already in progress, which will ultimately endow it with an additional accelerator (LCLS-II) equipped with superconducting accelerator cavities, and so bring the pulse repetition rate to about 1 MHz. For comparison, the currently operating source that employs a copper accelerator reaches a 120 Hz pulse rate. It will be, in fact, the first X-ray free-electron laser able to supply a uniformly-spaced train of pulses with programmable repetition rate.

As the two light sources will operate in parallel, the five existing beamlines will be maintained, plus three additional beamlines (TMO, TXI, and NEH 2.2) that will be located in the near experimental hutch (NEH).[2] The beam delivery to each beamline will be ensured by a front-end enclosure (FEE), equipped with bendable mirrors and a variable line spacing grating. The FEE is committed to perform the photon flux delivery without compromising its spatial and temporal coherence. To this end, the optical elements for moderating the beam shall exhibit excellent surface finishing and profile accuracy. Any surface defect would, in fact, leave an imprint in the wavefront propagation that will ultimately affect the coherence preservation and the final focusing performances in the beamlines, which should be close to the diffraction limit in order to fulfill the science requirements. This clearly sets stringent limits on the tolerances for the mirror fabrication.

The problem of determining the *necessary and sufficient* surface accuracy of optical components is probably as ancient as optical science itself. Providing a definite solution to that problem is, nevertheless, quite hard. The reason is that the propagation of X-rays is undulatory in nature, and the final focus in a chain of optical elements illuminated by *coherent* radiation is the result of a diffractive process series that often returns unintuitive results. The aberration imparted by a profile deformation always appears, for instance, mixed up with unavoidable diffraction features stemming from the mirror aperture, or by diffraction from the mirror surface roughness.

e-mail: spigasan@slac.stanford.edu, phone: +1-650-924-3070

Adaptive X-Ray Optics V, edited by Daniele Spiga, Hidekazu Mimura, Proc. of SPIE Vol. 10761, 1076107 · © 2018 SPIE · CCC code: 0277-786X/18/$18 · doi: 10.1117/12.2323253

Downloaded From: https://www.spiedigitallibrary.org/conference-proceedings-of-spie on 9/18/2018
Terms of Use: https://www.spiedigitallibrary.org/terms-of-use

Sometimes, the beam diffraction can make the geometric aberrations irrelevant, or enhance them, depending on their typical spatial scales and on the light wavelength λ. This makes not only the interpretation of tests, but also setting certain surface tolerances, quite complicated. A proper beamline equipment thereby requires simulation tools able to predict the impact of – either expected or measured – defects and misalignments of reflective surfaces. Possible input data for this tool are provided by metrology instruments such as the long trace profilometer (LTP),[3] phase shift interferometers (PSI), or wavefront sensors[4] to name a few.

In the past years, much effort was spent in preparing simulation tools that encompass the aspects of aperture diffraction, geometric deformations (usually analyzed via ray-tracing methods), and surface diffraction (usually treated via the first-order scattering theory).[5] A 1D wavefront propagation tool, named WISE (Wavefront propagatIon Simulation codE), was developed at INAF-OAB in recent years[6,7] to self-consistently simulate the expected performances in focusing optics for X-ray telescopes.[8] WISE was proven to affordably reproduce the focusing capabilities of Kirkpatrick-Baez (K-B) mirrors[9] at the *Fermi* free electron laser.[10] In addition, WISE has become part of the OASYS (OrAnge SYnchrotron Suite) software package,[11] enabling the capabilities of various ray-tracing[12–15] and wavefront propagation[10,16,17] simulation codes into a graphic environment for practical use.

However, in optical systems where the incidence plane changes along the beam propagation – as it is the case of K-B mirrors – a 2D simulation could be useful. The problem then becomes how to deal with the complexity of the computation, especially when surface defects over small spatial periods need to be included in the propagation, and the mirror surface to be processed is consequently represented by a very large matrix. As we will see in Sect. 2, this is simplified under the Fresnel approximation, which allows us to considerably speed up the computation, without strictly be in the far-field limit. This approach was, in fact, already adopted to successfully model the performances of normal-incidence mirrors for ground-based telescopes.[18] At a subsequent time, it was extended to a grazing-incidence geometry for simulating the diffraction pattern generated by silicon pore optics in the ATHENA X-ray telescope.[19]

In this paper, we adopt a similar method to approach 2D simulations of wavefront propagation in a coherent X-ray beamline. In Sect. 2, we analytically describe the basic treatment of elliptical mirrors, and we extend the reasoning to a double reflection, showing that the simulation can be extended to a sequence of mirrors. In Sect. 3, we briefly discuss the simulation tool we are writing to simulate the X-ray propagation through the optical element sequence (Sequential Code for Diffraction Simulation, SCDS). Finally, in Sect. 4, we review some examples of computation for a K-B system, including deformations or measured surface defects. Further developments of this work will include mirrors with different geometries and spectroscopic components, such as reflection gratings.

2. PHYSICAL OPTICS TREATMENT OF ELLIPTICAL MIRRORS

2.1 General aspects

In this section we introduce the method we are adopting to perform the simulation of a beamline, regarded as a sequential chain of diffractive elements. In fact, we will use either the "reflective" or the "diffractive" adjective as synonyms, because – assuming a constant reflectivity of each mirror over its entire surface – the reflection of X-rays by focusing surfaces can always be regarded as a diffractive process. In order to take advantage of the Fourier transform and quickly compute the diffraction integrals, we will need to suppose the optical elements to be separated by distances D that are much larger than the cross-sectional dimensions W of the diffractive surfaces. This condition is known as *Fresnel approximation* and allows us to considerably simplify expressions of the diffraction integrals, while still being less stringent than the Fraunhofer (far-field) regime.

A situation where the Fresnel approximation is *not* applicable is, for instance, the Wolter-I geometry[20] used in astronomical optics, in which the secondary segment is located a few millimeters (or less) past the primary mirror. In this case, we could not simplify the diffraction integrals and so reduce them to Fourier transforms. They can still be evaluated in a quite short time if the simulation is collapsed in the incidence plane of the mirrors, ignoring sagittal deformations. This was the approach followed in the 1D simulation code WISE.[10]

However, at synchrotrons, FELs, and lab sources, the diffracting elements are more spaced apart and the Fresnel approximation is *usually* applicable. In particular, we do not require that the Fresnel number $F = W^2/\lambda D$ be very small (a condition required in the far-field limit). We also neglect obliquity factors and the variation of

Downloaded From: https://www.spiedigitallibrary.org/conference-proceedings-of-spie on 9/18/2018
Terms of Use: https://www.spiedigitallibrary.org/terms-of-use

the $1/D$ dependence on the specific location on the mirror surface. This basically means that we can consider all the components as *phase plates* that simply introduce phase changes over their aperture pupil, and offers us the opportunity to perform 2D diffraction computations without excessively increasing the computational load. The electric fields can therefore be computed at the mirror apertures in sequence, from the first to the last mirror of the beamline.

For brevity, in this paper we limit ourselves to the case of two reflections on elliptic mirrors with orthogonal orientations, which form the widespread K-B geometry. However, the method works regardless of the number of mirrors and can also be applied to a complex beamline.

2.2 K-B mirrors: first diffraction

We model the primary and the secondary element of a K-B mirror separately. We consider the primary element as vertical, i.e., a flawless, elliptical profile in the xy plane, and planar along the xz plane (Fig. 1A). Therefore, the primary element only focuses in y direction and lets the beam diverge along z. Let the semi-major axis be a and the semi-focal distance be c: we initially set the image point at the origin and the source on the x-axis, at $x = -2c$. Following a widespread notation, we denote with p and q the distances from the source and the image, respectively, to the mirror center. By definition of an ellipse, rays in the xy plane have a total optical path $d_1 + d_2$ from the source to the image point, which equals $(p+q) = 2a$ regardless of d_2 (r_0 in the xy plane).

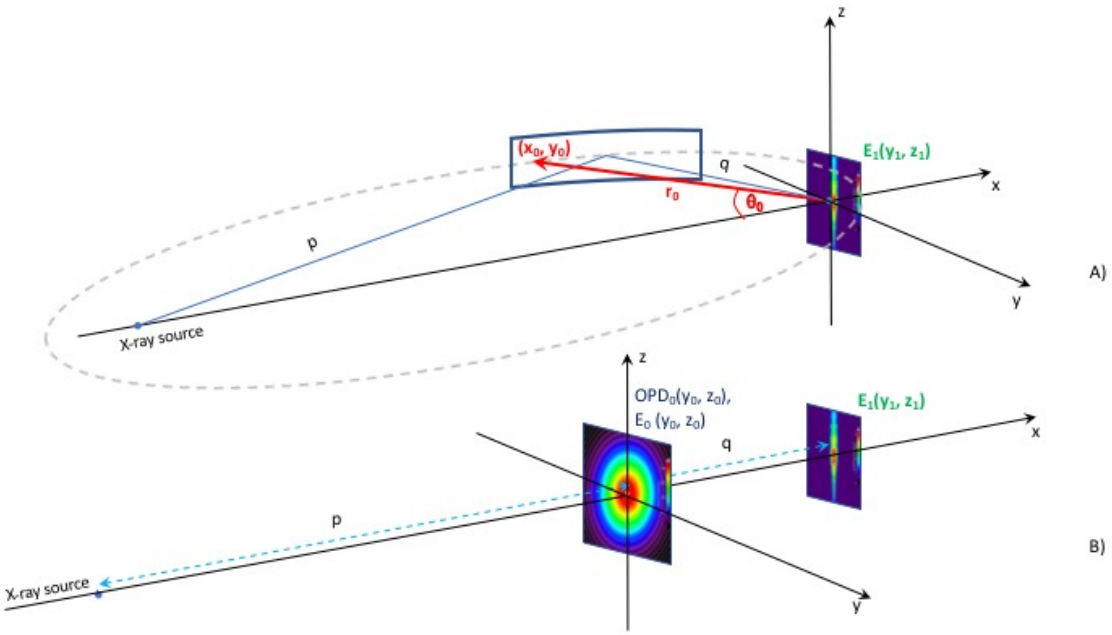

Figure 1. A) Initial reference frame used for the primary K-B element. The elliptical profile is described by the coordinates $x_0 = -r_0 \cos\theta_0$ and $y_0 = r_0 \sin\theta_0$, where $r_0 = a(1-e^2)/(1-e\cos\theta_0)$, a is the semi-major axis, c the semi-focal distance, and $e = c/a$ the ellipticity. B) Equivalent diffraction geometry, schematizing the mirror as a phase plate.

The optical path reaching the generic (x_0, y_0, z_0) location of the mirror is

$$d_1 = \sqrt{(-2c - x_0)^2 + y_0^2 + z_0^2} = \sqrt{4c\,(c - r_0\cos\theta_0) + r_0^2 + z_0^2}\,. \tag{1}$$

Handling now the ellipse equation (see caption of Fig. 1), we obtain $r_0\cos\theta_0 = (r_0 - a)/e + c$ and Eq. 1 turns into

$$d_1 = \sqrt{4a\,(a - r_0) + r_0^2 + z_0^2} = \sqrt{(2a - r_0)^2 + z_0^2} = \sqrt{(p + q - r_0)^2 + z_0^2}\ : \tag{2}$$

in the Fresnel approximation, we develop the square root in Eq. 2 at the first order, and we get

$$d_1 \simeq p + q - r_0 + \frac{z_0^2}{2(p + q - r_0)}. \tag{3}$$

Downloaded From: https://www.spiedigitallibrary.org/conference-proceedings-of-spie on 9/18/2018
Terms of Use: https://www.spiedigitallibrary.org/terms-of-use

To derive d_2, we consider an optical path reaching a detection area, centered in the nominal focus and described by the reference frame (y_1, z_1). The second distance, approximated at the first order, can be written as

$$d_2 = \sqrt{x_0^2 + (y_1 - y_0)^2 + (z_1 - z_0)^2} \simeq r_0 - \frac{y_0 y_1}{r_0} - \frac{z_0 z_1}{r_0} + \frac{y_1^2 + z_1^2}{2r_0} + \frac{z_0^2}{2r_0}, \tag{4}$$

and we can now combine Eqs. 3 and 4 to obtain the total optical path:

$$\mathrm{OPD}_1 = d_1 + d_2 \simeq (p+q) - \frac{y_0 y_1}{q} - \frac{z_0 z_1}{q} + z_0^2 \left(\frac{1}{2p} + \frac{1}{2q}\right) + \frac{y_1^2 + z_1^2}{2q}, \tag{5}$$

where we could set $r_0 \simeq q$ to a good approximation in all the denominators. For convenience, we now locate the reference frame at the mirror aperture. This particular choice does not affect the optical paths (Fig. 1B), but it will simplify the notation in the next steps. It can be also useful to rewrite Eq. 5 omitting unessential phase constants and separating the incident OPD_0 in the expression from the optical path shift (OPS_1) due to the mirror:

$$\mathrm{OPD}_1 = \underbrace{\frac{z_0^2 + y_0^2}{2p}}_{\mathrm{OPD}_0} \underbrace{- \frac{y_0 y_1}{q} - \frac{z_0 z_1}{q} + \frac{z_0^2}{2q} - \frac{y_0^2}{2p} + \frac{y_1^2 + z_1^2}{2q}}_{\mathrm{OPS}_1}. \tag{6}$$

Dubbing with $E_0(y_0, z_0)$ the electric field amplitude at the mirror aperture, the complex field diffracted to the focal plane is provided by the Fresnel-Kirchoff integral:

$$\mathcal{E}_1(y_1, z_1) = \frac{1}{\lambda q} \int E_0(y_0, z_0)\, e^{\frac{2\pi \mathrm{i}}{\lambda} \mathrm{OPD}_1}\, \mathrm{d}y_0 \mathrm{d}z_0, \tag{7}$$

that becomes, omitting obliquity factors,

$$\mathcal{E}_1(y_1, z_1) = \frac{e^{\frac{\pi \mathrm{i}}{\lambda q}(y_1^2 + z_1^2)}}{\lambda q} \int e^{-\frac{2\pi \mathrm{i}}{\lambda q} y_0 y_1}\, e^{-\frac{2\pi \mathrm{i}}{\lambda q} z_0 z_1} \left[E_0(y_0, z_0)\, e^{\frac{\pi \mathrm{i}}{\lambda} z_0^2 \left(\frac{1}{p} + \frac{1}{q}\right)}\right] \mathrm{d}y_0 \mathrm{d}z_0. \tag{8}$$

Equation 8 is just the Fourier transform of the term enclosed in [ ] brackets, and can be regarded as the diffraction through a phase plate, which introduced an OPS_1 into the path of the incident wave. This allows us to regard the mirror as a diffractive element along the x-axis (Fig. 1).

In the case of a Gaussian intensity wavefront, typical of FEL beams in the fundamental mode, we can set

$$E_0(y_0, z_0) = \frac{1}{\omega \sqrt{\pi/2}} \exp\left(-\frac{y_0^2 + z_0^2}{\omega^2}\right), \tag{9}$$

where the normalization constant was selected in order to normalize the electric field's squared module to unity on the $y_0 z_0$ plane. The ω parameter can be connected to the source profile rms, ω_0, via the relation $\omega \simeq \lambda p / \pi \omega_0$, which follows from the propagation theory of Gaussian beams under approximation $\omega \gg \omega_0$. Using the last relation and substituting Eq. 9, we can solve explicitly Eq. 8:

$$\mathcal{E}_1(y_1, z_1) = \frac{\sqrt{\pi}}{\lambda x_1 \gamma}\, e^{\frac{\pi \mathrm{i}}{\lambda x_1}(y_1^2 + z_1^2)}\, e^{-\left(\frac{p}{\omega_0 q}\right)^2 y_1^2}\, e^{-\left(\frac{\pi}{\lambda x_1 \gamma}\right)^2 z_1^2}, \tag{10}$$

having set $\gamma^2 = \omega^{-2} - \pi \mathrm{i}(1/p + 1/q)/\lambda$. Equation 10, after some algebraic reworking, takes the form

$$\mathcal{E}_1(y_1, z_1) \simeq \sqrt{\frac{2}{\pi}} \sqrt{\frac{p}{\omega_0 q}} \exp\left[-\left(\frac{p\, y_1}{\omega_0 q}\right)^2 + \mathrm{i} \frac{\pi y_1^2}{\lambda q}\right] \sqrt{\frac{p}{\omega(p+q)}} \exp\left[-\left(\frac{p\, z_1}{\omega(p+q)}\right)^2 + \mathrm{i} \frac{\pi z_1^2}{\lambda (p+q)}\right]: \tag{11}$$

and as expected, the first factor in Eq. 11 describes the image of the Gaussian source, demagnified by a factor q/p along y_1. The second factor represents, in contrast, the unperturbed (diverging) propagation of the Gaussian wavefront along the z_1 axis.

Downloaded From: https://www.spiedigitallibrary.org/conference-proceedings-of-spie on 9/18/2018
Terms of Use: https://www.spiedigitallibrary.org/terms-of-use

2.3 K-B mirrors: second diffraction

We now want to place the second (horizontal) K-B element in an intra-focal position of the vertical one, at a generic distance x_1 (Fig. 2). If we keep on mapping the second mirror aperture via the coordinates (y_1, z_1), we just have to re-write Eq. 5 replacing $q \to x_1$, plus an additional OPD that keeps the y-focus as a distance q from the primary mirror center, i.e., $y_0^2(1/2x_1 - 1/2q)$. Furthermore, we change the notation $p \to p_1$ and $q \to q_1$ for indicating the ellipse parameters of the first diffracting element. All this changes Eq. 8 into

$$\mathcal{E}_1(y_1, z_1) = \frac{e^{\frac{\pi \mathrm{i}}{\lambda x_1}(y_1^2+z_1^2)}}{\lambda x_1} \int e^{-\frac{2\pi \mathrm{i}}{\lambda x_1} y_0 y_1}\, e^{-\frac{2\pi \mathrm{i}}{\lambda x_1} z_0 z_1} \left[E_0(y_0, z_0)\, e^{\frac{\pi \mathrm{i}}{\lambda}\left(\frac{q_1 - x_1}{x_1 q_1}\, y_0^2 + \frac{p_1 + x_1}{x_1 p_1}\, z_0^2\right)} \right] \mathrm{d}y_0 \mathrm{d}z_0. \tag{12}$$

Using Eq. 9, we can solve Eq. 12 in a few passages, obtaining

$$\mathcal{E}_1(y_1, z_1) = \frac{\sqrt{\pi}}{\omega \lambda x_1 \alpha_y \alpha_z}\, e^{\frac{\pi \mathrm{i}}{\lambda x_1}(y_1^2+z_1^2)}\, e^{-\left(\frac{\pi}{\lambda x_1 \alpha_y}\right)^2 y_1^2}\, e^{-\left(\frac{\pi}{\lambda x_1 \alpha_z}\right)^2 z_1^2}, \tag{13}$$

where the two complex propagation constants α_y and α_z are provided by the relations:

$$\alpha_y^2 = \frac{1}{\omega^2} - \mathrm{i}\frac{\pi}{\lambda x_1}\frac{q_1 - x_1}{q_1}, \tag{14}$$

$$\alpha_z^2 = \frac{1}{\omega^2} - \mathrm{i}\frac{\pi}{\lambda x_1}\frac{p_1 + x_1}{p_1}, \tag{15}$$

and we also note that, if $x_1 = q_1$, then $\alpha_y = 1/\omega$ and Eq. 13 ultimately reduces to Eq. 10. Equation 13 describes the electric field on the aperture pupil of the second K-B segment, but only if the wavefront from the source is initially spherical, i.e. characterized by an OPD_0 term as in Eq. 6.

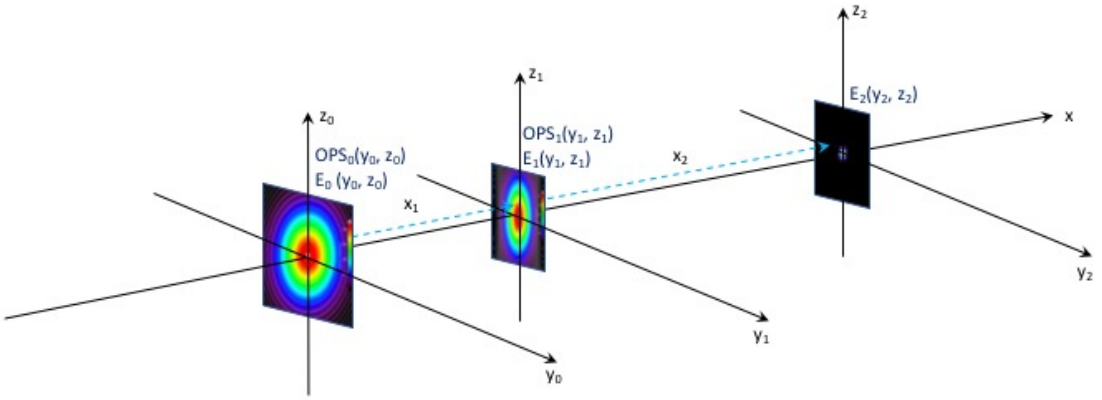

Figure 2. A diffracting system equivalent to the two elements of a K-B mirror. Every mirror element is described by its specific optical phase shift (OPS).

However, if we absorb the phase information of the incident wave into a more general complex incident field $\mathcal{E}_0(y_0, z_0)$, we can write a general expression for the field after the first diffraction,

$$\mathcal{E}_1(y_1, z_1) = \frac{e^{\frac{\pi \mathrm{i}}{\lambda x_1}(y_1^2+z_1^2)}}{\lambda x_1} \int e^{-\frac{2\pi \mathrm{i}}{\lambda x_1} y_0 y_1}\, e^{-\frac{2\pi \mathrm{i}}{\lambda x_1} z_0 z_1} \left[\mathcal{E}_0(y_0, z_0)\, e^{\frac{\pi \mathrm{i}}{\lambda}\left(\frac{1}{x_1} - \frac{1}{p_1} - \frac{1}{q_1}\right) y_0^2}\, e^{\frac{\pi \mathrm{i}}{\lambda x_1} z_0^2} \right] \mathrm{d}y_0 \mathrm{d}z_0, \tag{16}$$

where only the OPS_1 terms (Eq. 6) appear in the exponents of the integrand. We now can compute the electric field diffracted by the second (horizontal) K-B mirror element to focus, at x_2 distance (Fig. 2). We simply move the reference frame origin into the x_1 coordinate and rewrite Eq. 16, after reversing the roles of y and z in the integrand:

$$\mathcal{E}_2(y_2, z_2) = \frac{e^{\frac{\pi \mathrm{i}}{\lambda x_2}(y_2^2+z_2^2)}}{\lambda x_2} \int e^{-\frac{2\pi \mathrm{i}}{\lambda x_2} y_1 y_2}\, e^{-\frac{2\pi \mathrm{i}}{\lambda x_2} z_1 z_2} \left[\mathcal{E}_1(y_1, z_1)\, e^{\frac{\pi \mathrm{i}}{\lambda}\left(\frac{1}{x_2} - \frac{1}{p_2} - \frac{1}{q_2}\right) z_1^2}\, e^{\frac{\pi \mathrm{i}}{\lambda x_2} y_1^2} \right] \mathrm{d}y_1 \mathrm{d}z_1. \tag{17}$$

Downloaded From: https://www.spiedigitallibrary.org/conference-proceedings-of-spie on 9/18/2018
Terms of Use: https://www.spiedigitallibrary.org/terms-of-use

The result can be extended to an arbitrary number of diffractions involving elliptical mirrors. If the K-B is correctly configured to minimize astigmatism effects, then we shall have the conditions $p_2 = p_1 + x_1$ and $q_1 = q_2 + x_1$ fulfilled. The image in seen in focus when $x_2 = q_2$. Finally, if the shape deviates from a perfect ellipse, due to manufacturing errors or deliberate adaptation to wavefront, the deformation can be accounted for in the computation (Eqs. 27 and 28, and Sect. 4.2).

In the case of a flawless, in-focus K-B system we can rewrite Eq. 17 as

$$\mathcal{E}_2(y_2, z_2) = \frac{e^{\frac{\pi \mathrm{i}}{\lambda q_2}(y_2^2+z_2^2)}}{\lambda q_2} \int e^{-\frac{2\pi \mathrm{i}}{\lambda q_2} y_1 y_2} \left[\mathcal{E}_1(y_1, z_1)\, e^{-\frac{\pi \mathrm{i}}{\lambda p_2} z_1^2} e^{\frac{\pi \mathrm{i}}{\lambda q_2} y_1^2}\right] \mathrm{d}y_1 \mathrm{d}z_1. \tag{18}$$

Substituting the expression for $\mathcal{E}_1$ (Eq. 13), α_y^2 (Eq. 14), and α_z^2 (Eq. 15), one gets (after considerable handling):

$$\mathcal{E}_2(y_2, z_2) = \frac{\sqrt{\pi} e^{\frac{\pi \mathrm{i}}{\lambda q_2}(y_2^2+z_2^2)}}{\lambda^2 \omega x_1 q_2 \alpha_y \alpha_z} \int e^{-\frac{2\pi \mathrm{i}}{\lambda q_2} y_1 y_2}\, e^{-\frac{2\pi \mathrm{i}}{\lambda q_2} z_1 z_2}\, e^{-\left(\frac{y_1}{\beta_y}\right)^2} e^{-\left(\frac{z_1}{\beta_z}\right)^2} \mathrm{d}y_1 \mathrm{d}z_1, \tag{19}$$

where the two complex constants β_y, β_z are provided by

$$\beta_y^2 = \omega^2 \left(\frac{q_2}{q_1}\right)^2 + \mathrm{i}\frac{\lambda x_1 q_2}{\pi q_1} \qquad \beta_z^2 = \omega^2 \left(\frac{p_2}{p_1}\right)^2 + \mathrm{i}\frac{\lambda x_1 p_2}{\pi p_1}. \tag{20}$$

Equation 19 can be solved immediately and, recalling the relation $\omega \simeq \lambda p_1 / \pi \omega_0$, the final expression is

$$\mathcal{E}_2(y_2, z_2) = \sqrt{\frac{2}{\pi}} \sqrt{\frac{p_1}{\omega_0 q_1}} e^{-\left(\frac{p_1}{\omega_0 q_1}\right)^2 y_2^2 + \mathrm{i}\frac{\pi y_2^2}{\lambda q_1}} \sqrt{\frac{p_2}{\omega_0 q_2}} e^{-\left(\frac{p_2}{\omega_0 q_2}\right)^2 z_2^2 + \mathrm{i}\frac{\pi z_2^2}{\lambda q_2}}, \tag{21}$$

i.e., the Gaussian profile of the source, demagnified by a factor of q_1/p_1 along y and q_2/p_2 along z. We note that – as expected – the squared module of Eq. 21 is normalized to 1, just like the one of the incident field.

3. NUMERICAL IMPLEMENTATION

While the behavior of an ideal K-B mirror can already be predicted analytically (Eq. 21), it might be interesting to have available a numerical tool able to perform a sequential simulation of the real mirrors, including profile and surface errors. This can be achieved by performing the integrations numerically. In particular, as they essentially involve Fourier transforms, for which efficient routines exist in virtually all programming languages, the computation can be made last only a few minutes using a commercial computer. Additionally, the results shown in the previous section can be used to simulate a sequence of N elliptical mirrors labeled with n = 0,1, ..., $N-1$, with either vertical (Eq. 16) or horizontal (Eq. 17) orientation. The final image is detected on a simulated CCD in the N-th place of the sequence.

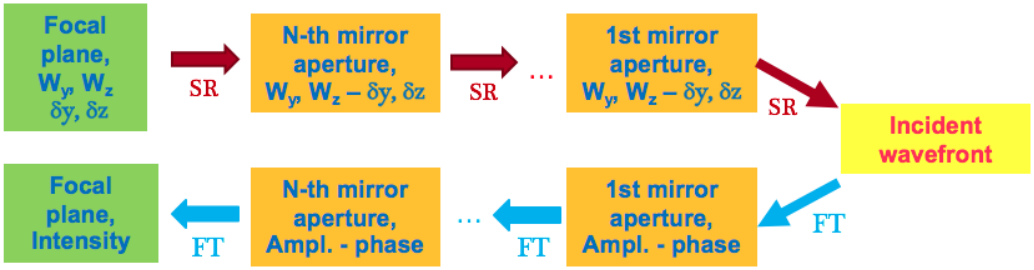

Figure 3. Schematic flow chart of SCDS. The first step consists in determining the optimal sampling and windowing of the matrices including the physical apertures of the mirrors. To this end, the sampling rules (SR, Eqs. 22 through 25) are used up to the incident wavefront. In the second step, the diffracted electric fields are computed in rapid sequence by means of Fourier transforms (FT, Eqs. 27 and 28).

The Fourier transform efficiency is essentially determined by the size of the matrix to be processed. This is in turn affected by two factors: the mirror aperture size and the mirror aperture sampling step (that can

Downloaded From: https://www.spiedigitallibrary.org/conference-proceedings-of-spie on 9/18/2018
Terms of Use: https://www.spiedigitallibrary.org/terms-of-use

also be different along y and z). The n-th aperture pupil y-size, $W_{y,n}$, shall obviously include the full mirror extent along y, $Y_{\mathrm{mir},n}$. However, it should also be large enough to have the diffraction limit resolved by the sampling step[18,19] of the next aperture pupil, located at a distance x_{n+1}. This condition basically ensures that the diffraction pattern has sufficient detail to fully exploit the capabilities of the imaging system.

The n-th aperture pupil y-sampling step, δy_n, is determined according to similar criteria: on a side, it should be smaller than $\delta y_{\mathrm{err},n}$, the lateral scale of the finest surface defect that has to be included in the computation, projected on the aperture pupil. On the other side, the sampling step should be sufficiently tight to enable diffraction throughout the full field of the $n+1$-th aperture. Identical statements can be made for the aperture size and sampling along z. We can therefore recapitulate the aforementioned requirements into the sampling rules:

$$W_{y,n} = \max\left(Y_{\mathrm{mir},n}\,;\lambda\frac{x_{n+1}}{\delta y_{n+1}}\right), \tag{22}$$

$$W_{z,n} = \max\left(Z_{\mathrm{mir},n}\,;\lambda\frac{x_{n+1}}{\delta z_{n+1}}\right), \tag{23}$$

$$\delta y_n = \min\left(\delta y_{\mathrm{err},n}\,;\lambda\frac{x_{n+1}}{W_{y,n+1}}\right), \tag{24}$$

$$\delta z_n = \min\left(\delta z_{\mathrm{err},n}\,;\lambda\frac{x_{n+1}}{W_{z,n+1}}\right), \tag{25}$$

which allow us to recursively determine the full sequence of mirror apertures upstream (Fig. 3), from the final detector ($W_{y,N}$, $W_{z,N}$, δy_N, δz_N) to the wavefront incident onto the first mirror ($W_{y,0}$, $W_{z,0}$, δy_0, δz_0).

The second step (Fig. 3) consists in the downstream computation of the electric field from the 0-th to the N-th aperture, using the Fourier transform based expressions. The construction of the apertures using the sampling rules (Eqs. 22–25) then ensures that each simulated diffraction will be properly imaged to a resolution equal or higher than requested by the next diffractive element *and* mapped over an area that is equal or larger than the aperture of the next diffractive element. While having a larger aperture area can be simply managed by trimming the aperture frame to the $(W_{y,n}, W_{z,n})$ size, a higher resolution will simply entail, at the subsequent step, a diffraction map over an area larger than the designed aperture initially. The exceeding frame of the diffracted pattern can therefore be trimmed harmlessly, before the next Fourier transform is carried out.

Imperfect mirrors can be simulated also. To this end, we denote with $\epsilon(y_n, z_n)$ the n-th mirror error map in the sequence, either measured or modeled (e.g., from a power spectral density[6]) and projected onto the aperture pupil. Then the electric field diffracted by the imperfect mirror is obtained from Eq. 16 and/or Eq. 17, after multiplying the integrand into the complex pupil function:

$$C_{err}(y_n, z_n) = \exp\left[-\frac{2\pi\mathrm{i}}{\lambda}\,2\epsilon(y_n, z_n)\sin\theta_n\right], \tag{26}$$

where θ_n is the grazing incidence angle, and the minus sign has been added to the exponent because a *positive* elevation on the surface actually *shortens* the optical path. This method has already been adopted to account for surface perturbations in near-normal incidence mirrors, with excellent agreement between experiment and simulations in near-infrared light.[18] It is essential, however, that the aperture pupil sampling step be tight enough to have the lateral scale of surface defects duly represented in ϵ (Eqs. 24 and 25). With some minor changes, this method can also be applied to diffractive-reflective components such as gratings. The $\epsilon(y_n, z_n)$ function would simply represent the profile (blazed, laminar, ...) of the grating.

We can therefore generalize Eqs. 16 and 17 as follows:

$$\mathcal{E}_1(y_1, z_1) = \frac{e^{\frac{\pi\mathrm{i}}{\lambda x_1}(y_1^2+z_1^2)}}{\lambda x_1}\;\widehat{\mathrm{FT}}\left[\mathcal{E}_0(y_0, z_0)\,C_{err1}(y_0, z_0)\,e^{\frac{\pi\mathrm{i}}{\lambda}\left(\frac{1}{x_1}-\frac{1}{f_1}\right)y_0^2}\,e^{\frac{\pi\mathrm{i}}{\lambda x_1}z_0^2}\right], \tag{27}$$

$$\mathcal{E}_2(y_2, z_2) = \frac{e^{\frac{\pi\mathrm{i}}{\lambda x_2}(y_2^2+z_2^2)}}{\lambda x_2}\;\widehat{\mathrm{FT}}\left[\mathcal{E}_1(y_1, z_1)\,C_{err2}(y_1, z_1)\,e^{\frac{\pi\mathrm{i}}{\lambda}\left(\frac{1}{x_2}-\frac{1}{f_2}\right)z_1^2}\,e^{\frac{\pi\mathrm{i}}{\lambda x_2}y_1^2}\right]. \tag{28}$$

Downloaded From: https://www.spiedigitallibrary.org/conference-proceedings-of-spie on 9/18/2018
Terms of Use: https://www.spiedigitallibrary.org/terms-of-use

where we have shortly defined $1/f_1 = 1/p_1 + 1/q_1$, $1/f_2 = 1/p_2 + 1/q_2$, and we have explicitly indicated the complex pupil functions of the mirror errors. We have coded this algorithm into SCDS and we have applied it to the preliminary case of a K-B system. The simulation results are displayed in the next section.

4. SIMULATION RESULTS FOR A K-B MIRROR

4.1 Perfect system

The first example we show here essentially reproduces the analytical results obtained in Sect. 2.3. We have considered the Gaussian beam at LCLS in the fundamental mode and simulated its incidence on a K-B mirror, at 0.3, 0.7, and 1.0 keV. We have assumed realistic parameters for this example, but it should be kept in mind

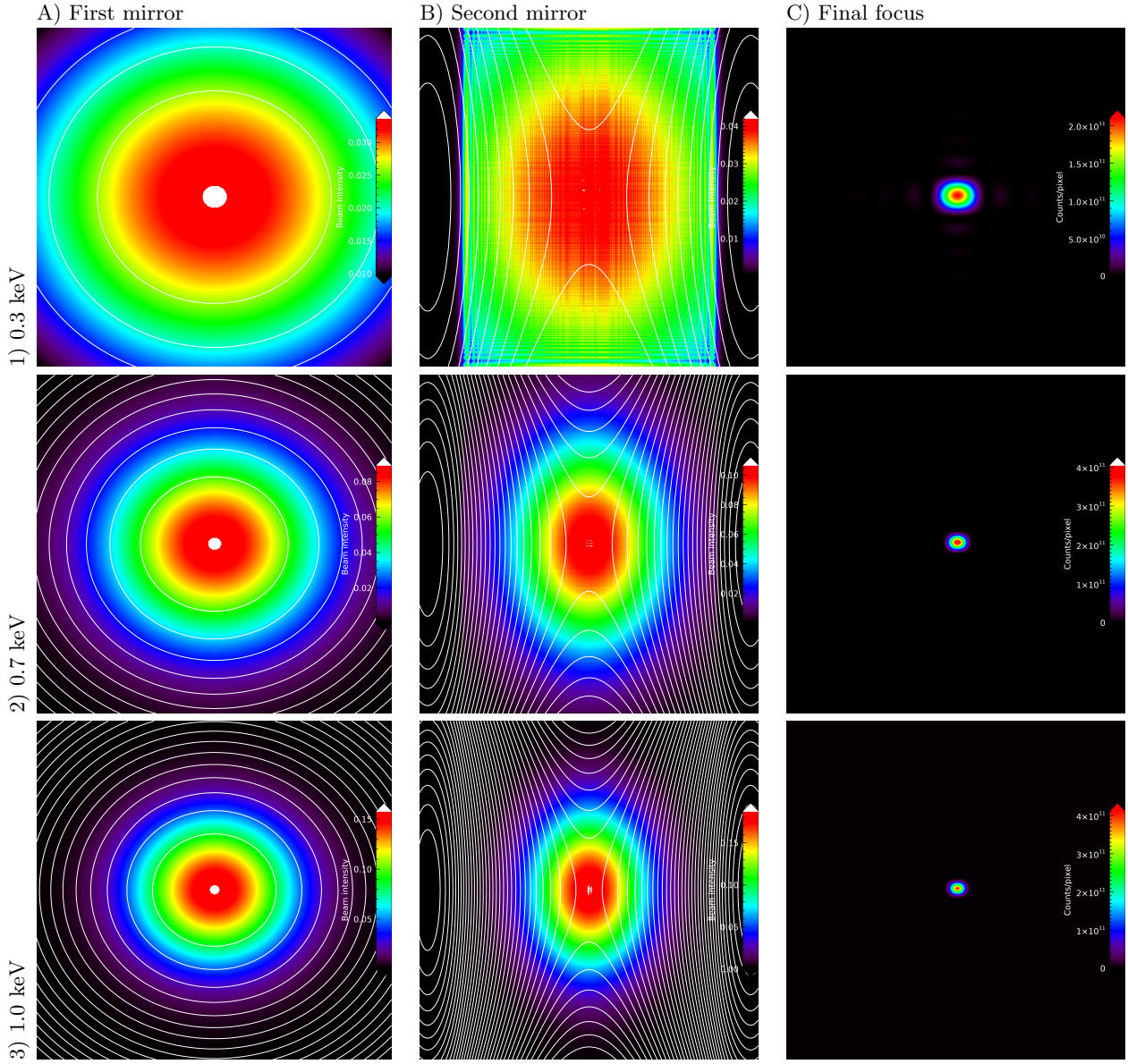

Figure 4. SCDS results for the LCLS Gaussian beam, focused by a K-B system, at three different energies. A) Vertical mirror aperture, 5.3 mm × 5 mm. B) Horizontal mirror aperture, 5 mm × 5.3 mm. C) Nominal focus, image size 0.25 mm× 0.25 mm. Shades of color denote the normalized intensity, while white lines connect equal phase points: consecutive lines are separated by a 6π phase difference.

Downloaded From: https://www.spiedigitallibrary.org/conference-proceedings-of-spie on 9/18/2018
Terms of Use: https://www.spiedigitallibrary.org/terms-of-use

that this is just a test case. The two mirror elements have both a reflective surface that is 250 mm long and 5 mm wide, with a central incidence angle of 21 mrad. The first mirror, located upstream, has the reflective surface oriented vertically, characterized by the parameters p_1, q_1. The second mirror is downstream and has the ellipse parameters p_2, q_2. Because the source location depends on the X-ray energy and is always supposed to be in the first mirror focus, p_1 is made vary with the energy also. The mirror separation ($x_1 = 5120$ mm from center to center) is kept fixed in all the simulations, so p_2 changes accordingly. In contrast, we assume the final detector in fixed position: hence, $q_1 = 26000$ mm and $q_2 = 20880$ mm are kept constant throughout all the simulations.

Energy (keV)	p_1 (mm)	p_2 (mm)	Divergence (μrad)	Source (μm)	Demag. source (μm, h.× v.)	Image (μm, h.× v.)	Collected power
0.3 keV	109160	114280	49.3	41.9	10.0×7.7	19.0×14.7	94%
0.7 keV	101760	106880	24.3	36.5	9.3×7.2	9.5×7.4	99%
1.0 keV	97660	102780	18.0	34.4	9.1×7.0	8.4×6.4	100%

Table 1. Summary of the parameter values used for simulating the perfect K-B system. The data are referred to the superconducting accelerator being built at LCLS, and to the soft X-ray undulator. All the widths are FWHM values. At 0.7 and 1 keV, the discrepancies between the predicted and the simulated image width (Fig. 4, col. C) are smaller than the pixel size (2 μm) adopted in the computation.

Owing to the self-diffraction of the Gaussian beam, the beam width on the first mirror aperture changes with λ. The beam divergence FWHMs at each X-ray energy under test are listed in Table 1, along with the source width and the expected image width from the demagnification ratios $q_1/p_1, q_2/p_2$. Assuming a final detector area of 250 μm × 250 μm with 2 μm resolution in both directions, the computation of the focused image just took ∼300 s per energy, using a commercial computer equipped with a 2.8 GHz processor and a 16 GB RAM. The aperture sizes and resolutions were inferred from the sampling rules in Sect. 3, yielding a maximum matrix size of 8500 × 8500, and a 0.6 μm resolution on the vertical mirror aperture.

The simulation results are shown in Fig. 4: the color scale describes the intensity distribution, whereas the white lines describe the intersection of some wavefronts with the aperture planes. At 0.3 keV, the beam is actually broader than the modeled mirror aperture (Fig. 4,A1), and part of the beam is not collected. As a consequence of the Gaussian tail cut-offs, diffraction fringes became visible in the diffracted pattern on the second aperture (Fig. 4,B1), and the doubly-diffracted image (Fig. 4,C1) appears rectangular instead of circular, with some emerging diffraction fringes at the four sides. Therefore, the focal spot is considerably broader than it would be expected from geometric considerations (Table 1).

At 0.7 keV and 1.0 keV (Fig. 4, rows 2 and 3), the beam is almost completely collected within the aperture of both mirror segments. As it could be expected, no diffraction fringes are visible after the first diffraction or in the final focus (Fig. 4,C2 and Fig. 4,C3). The latter reproduces, in fact, the Gaussian profile of the source, including the typical distortion of K-B mirrors (anamorphism) caused by the different locations of the vertical and the horizontal element. The image FWHMs are, in these two cases, very close to the ones of the demagnified source (Table 1).

4.2 Deviation from perfect profile

As a further exercise, we have repeated the simulation at 0.7 keV including two kinds of profile errors: a tangential profile measured by an LTP on a test mirror, and an hypothetic sagittal curvature error.

The tangential error profile under test (Fig. 5) is a quite smooth one: in fact, with a profile rms of 71 nm and an incidence angle of 21 rad, the projected height is comparable with λ, so we cannot expect the geometric optics to be applicable. Physical optics, however, has general validity and we can so assess easily the effect of this perturbation on the focal spot. After resampling the profile at the actual aperture sampling steps and using Eq. 26 to evaluate C_{err} for both mirror segments, we obtained the diffraction patterns shown in Fig. 6,

Downloaded From: https://www.spiedigitallibrary.org/conference-proceedings-of-spie on 9/18/2018
Terms of Use: https://www.spiedigitallibrary.org/terms-of-use

row 1. After the first diffraction (B1), the profile has considerably perturbed the Gaussian intensity, but also the wavefronts appear deformed. The intensity now exhibits a modulation, almost completely along the incidence plane (horizontal), superimposed to the usual Gaussian shape. After the second diffraction, the same modulation has also appeared along the vertical axis, with enhanced high orders of diffraction around the central focus.

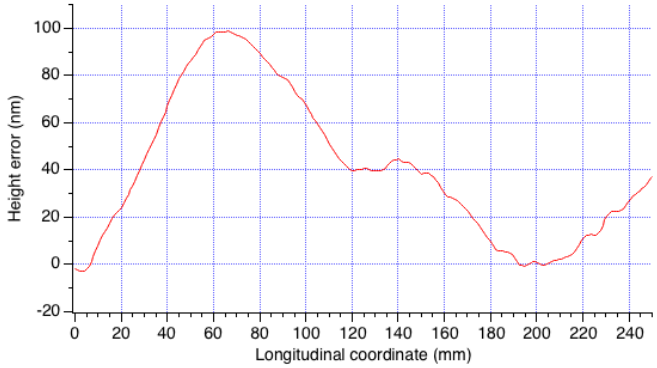

Figure 5. Mirror profile errors used in the simulation of Fig. 6, row 1.

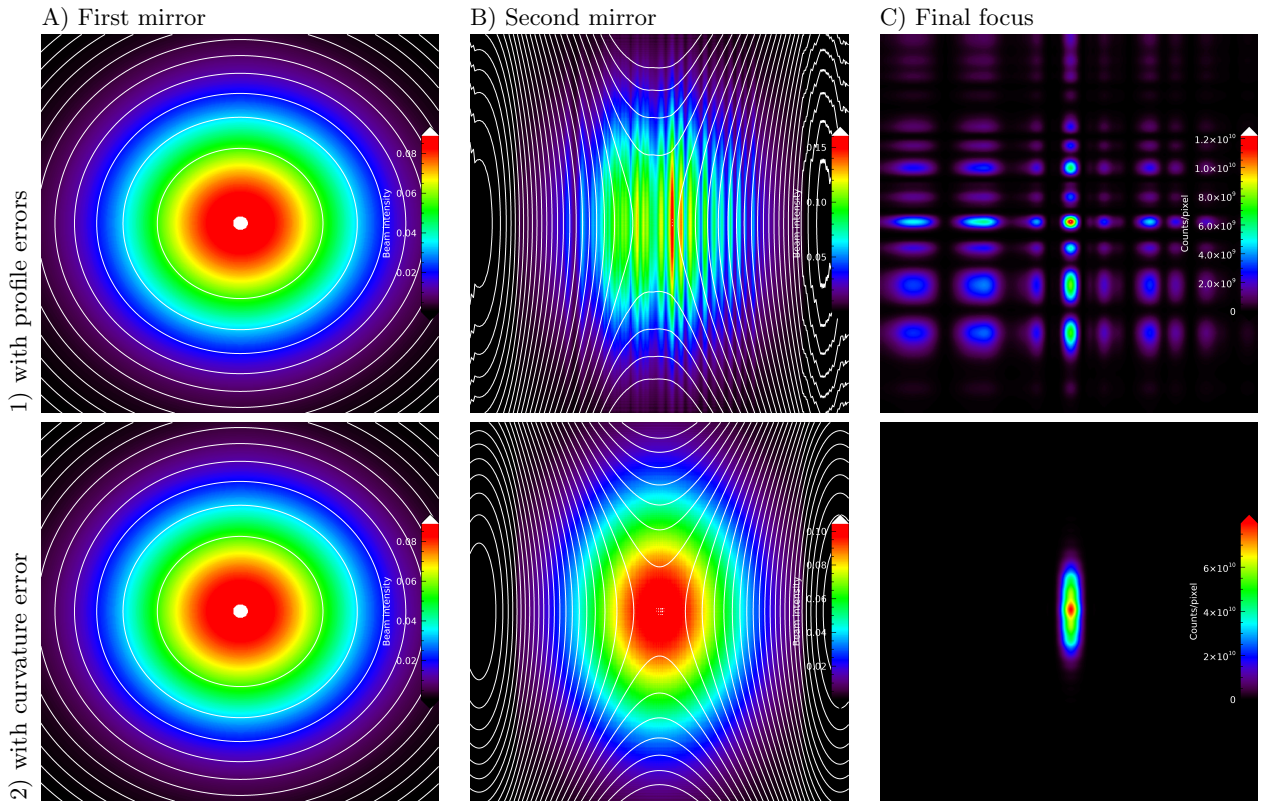

Figure 6. SCDS results for the LCLS Gaussian beam, focused by a K-B system, at 0.7 keV, examples of imperfect mirrors (to be compared with Fig. 4). A) Vertical mirror aperture, 5.3 mm × 5 mm. B) Horizontal mirror aperture, 5 mm × 5.3 mm. C) Nominal focus, image size 0.25 mm× 0.25 mm. 1) vertical and horizontal mirror with profile errors as shown in Fig. 5. 2) vertical mirror segment with a sagittal radius of curvature of 50 m.

As for the second simulation, we have this time assumed no tangential defect. We have supposed that the vertical mirror, instead of being planar along the sagittal direction, be laterally bent to a 50 m radius of curvature. After turning this information into a height profile error ϵ, we have re-run the diffraction algorithm and obtained

Downloaded From: https://www.spiedigitallibrary.org/conference-proceedings-of-spie on 9/18/2018
Terms of Use: https://www.spiedigitallibrary.org/terms-of-use

the diffraction patterns in Fig. 6, row 2. While no relevant change is seen after the first diffraction, the image in focus (Fig. 6,C2) appears elongated vertically (FWHM = 42.5 μm) by the same amount that could be computed from geometric optics (FWHM = 44 μm). The residual discrepancy is caused by the finite spatial sampling of the modeled detector.

5. CONCLUSIONS

In this paper, we have shown how 2D simulation of a coherent X-ray wavefront propagation through a beamline can be achieved replacing the reflective elements with appropriate phase plates, and demanding all the computation to a sequence of Fourier transforms. The involved approximations simply require that the optical components be not too close to each other, a situation usually met in FEL beamlines. We have so far applied the method to a K-B mirror system. The diffracted electric field after two reflections (Fig. 2) can be obtained applying Eqs. 27 and 28 in sequence: if the aperture pupils are properly sized and sampled, the full computation takes only a few minutes. After implementing the procedure in SCDS, we have reported some examples showing how the numerical elaboration is working properly. Future work will be aimed at simulating the entire FEE of LCLS-II and the beamlines, including reflection gratings and planar mirrors.

ACKNOWLEDGMENTS

This work is supported by US Department of Energy Office of Science.

REFERENCES

[1] Cocco, D., Abela, R., Amann, J.W., Chow, K.P., Emma, P.J., Feng, Y., Gassner, G.L., Hastings, J.B., Heimann, P.A., Huang, Z., Kelez, N.M., Loos, H., Montanez, P.A., Morton, D.S., Nuhn, H.D., Ratner, D.F., Rodes, L.N., Flechsig, U., Welch, J.J. and Wu, J., "The optical design of the soft x-ray self seeding at LCLS," Proc. SPIE 8849, 88490A (2013)

[2] https://lcls.slac.stanford.edu/instruments/l2si

[3] Takacs, P.Z., Qian, S. and Colbert, J., "Design Of A Long Trace Surface Profiler," Proc. SPIE 749 (1987)

[4] Cocco, D., Idir, M., Morton, D., Raimondi, L. and Zangrando, M., "Advances in X-ray optics: From metrology characterization to wavefront sensing-based optimization of active optics," NIM-A, in press (2018)

[5] Church, E. L., Jenkinson, H. A. and Zavada, J. M., "Measurement of the finish of diamond-turned metal surfaces by differential light scattering," Optical Engineering 18, 125 (1979)

[6] Spiga, D. and Raimondi, L., "X-ray optical systems: from metrology to Point Spread Function," Proc. SPIE 9209, 92090E (2014)

[7] Raimondi, L. and Spiga, D., "Mirrors for X-ray telescopes: Fresnel diffraction-based computation of point spread functions from metrology," Astron. Astrophys. 573, A22(2015)

[8] Spiga, D., Raimondi, L., Furuzawa, A., Basso, S., Binda, R., Borghi, G., Cotroneo, V., Grisoni, G., Kunieda, H., Marioni, F., Matsumoto, H., Mori, H., Miyazawa, T., Negri, B., Orlandi, A., Pareschi, G., Salmaso, B., Tagliaferri, G., Uesugi, K., Valsecchi, G. and Vernani, D., "Angular resolution measurements at SPring-8 of a hard x-ray optic for the New Hard X-ray Mission," Proc. SPIE 8147, 81470A (2011)

[9] Kirkpatrick, P. and Baez, A.V., "Formation of Optical Images by X-Rays," Journal of the OSA 38(9), 766 (1948)

[10] Raimondi, L., Svetina C., Mahne N., Cocco D., Abrami A., De Marco M., Fava C., Gerusina S., Gobessi R., Capotondi F., Pedersoli E., Kiskinova M., De Ninno G., Zeitoun P., Dovillaire G., Lambert G., Boutu W., Merdji H., Gonzalez A.I., Mahieu B., Gauthier D. and Zangrando M., "Microfocusing of the FERMI@Elettra FEL beam with a K-B active optics system: spot size predictions by application of the WISE code," NIM-A 710, 131 (2013)

[11] Rebuffi, L. and Sanchez del Rio, M., "OASYS (OrAnge SYnchrotron Suite): an open-source graphical environment for x-ray virtual experiments," Proc. SPIE 10388, 103880S (2017)

[12] Sanchez del Rio, M., Canestrari, N., Jiang, F. and Cerrina, F., "SHADOW3: a new version of the synchrotron X-ray optics modelling package," Journal of Synchrotron Radiation, 18, 708-716 (2011)

Downloaded From: https://www.spiedigitallibrary.org/conference-proceedings-of-spie on 9/18/2018
Terms of Use: https://www.spiedigitallibrary.org/terms-of-use

[13] Schäfers, F., [Modern Developments in X-Ray and Neutron Optics, Springer Series in Modern Optical Sciences], Springer-Verlag, Berlin Heidelberg, 137, 9 (2008)

[14] Klementiev, L. K., "A powerful scriptable ray tracing package xrt," Proc. SPIE 9209, 920909 (2014)

[15] Bergbäck Knudsen, E., Prodi, A., Baltser, J., Thomsen, M., Kjaer Willendrup, P., Sanchez del Rio, M., Ferrero, C., Farhi, E., Haldrup, K., Vickery, A., Feidenhansal, R., Mortensen, K., Meedom Nielsen, M., Friis Poulsen, H., Schmidt, S. and Lefmann, K., "McXtrace: a Monte Carlo software package for simulating X-ray optics, beamlines and experiments," Journal of Applied Crystallography 46, 679-696 (2013)

[16] Chubar, O. and Elleaume, P., "Accurate And Efficient Computation Of Synchrotron Radiation In The Near Field Region," Proceedings of the EPAC98 Conference, 22-26 June 1998, 1177-1179 (1998)

[17] Bahrdt, J., Flechsig, U., Grizolli, W. and Siewert F., "Propagation of coherent light pulses with PHASE," Proc. SPIE 9209, 920908 (2014)

[18] Tayabaly, K., Spiga, D., Sironi, G., Pareschi, G. and Lavagna, M., "Two-dimensional PSF prediction of multiple-reflection optical systems with rough surfaces," Proc. SPIE 9961, 99610N (2016)

[19] Spiga, D., Della Monica Ferreira, D., Shortt, B., Bavdaz, M., Bergback Knudsen, E., Bianucci, G., Christensen, F., Civitani, M. , Collon, M., Conconi, P., Fransen, S., Marioni, F., Massahi, S., Pareschi, G., Salmaso, B., S Jegers, A., Tayabaly, K., Valsecchi, G., Westergaard, N. and Wille, E., "Optical simulations for design, alignment, and performance prediction of silicon pore optics for the ATHENA x-ray telescope," Proc. SPIE 10399, 103990H (2007)

[20] Van Speybroeck, L.P. and Chase, R.C., "Design parameters of paraboloid-hyperboloid telescopes for X-ray astronomy," Appl. Opt. 11(2), 440 (1972)

Downloaded From: https://www.spiedigitallibrary.org/conference-proceedings-of-spie on 9/18/2018
Terms of Use: https://www.spiedigitallibrary.org/terms-of-use